Ionomigration of Neutral Phases in Ionic Conductors

I.-Wei Chen, Seung-Wan Kim, Ju Li, Suk-Joong L. Kang, and Fuqiang Huang*

Without sensing any physical force, a neutral object in an ion conducting solid can move in a uniform electrochemical field by coupling a global ion wind with localized counterion diffusion at the interface. This happens to pores and gas bubbles at 840 °C in a fast O^{2-} conductor, yttria-stabilized zirconia (YSZ), despite having cations that are essentially frozen with lattice diffusivities 10^{12} times slower than the O^{2-} diffusivity. Through-thickness migration and massive electro-sintering in thin YSZ ceramics are observed at voltages similar to those in YSZ fuel cells and electrolysis cells. This effect should apply to any electrochemically-loaded multiphase ionic conducting solid, with or without an electric field, and can lead to electrolyte sintering, phase accumulation and electrode debonding, resulting in unexpected benefit or damage in electrochemical devices. As the velocity obeys a pseudo Stokes-Einstein equation, inversely proportional to the object size, an especially enhanced size effect is expected in nanocomposites.

1. Introduction

Unexpected movement of inclusions (e.g., second phase particles or pores) due to an external field can have dramatic outcomes. In metal interconnects of integrated circuits, an electron wind transfers momentum to atoms, causing neutral voids to migrate and interconnects to break.[1] Momentum transfers by moving ions in biological liquids can push neutral nonelectrolytes (like water) around;[2] even counter ions can be dragged along when tethered to the moving ions by a linker (a protein called cotransporter),[3] giving rise to neutral salt migration. Energy gradients can also cause inclusions to migrate. For example, in a temperature gradient, heat of transport associated with ionic "molecules" (e.g., UO_2 in nuclear fuel) causes fission-gas bubbles to relocate, thus hollows the fuel core, initiates columnar grain growth and displaces fuel elements.[4] Likewise, in a graded electric/magnetic field, a neutral object migrates because its induced dipole is drawn into the high-field region, thus allowing fluid demixing[5] and object manipulation by electrical/magnetic/optical tweezers.[6] But without any energy gradient or momentum transfer, can a neutral inclusion in a perfectly ionic crystal (i.e., without electronic conductivity) move under a uniform electric field? This question is fundamentally important for such electrochemical devices as solid oxide fuel cell (SOFC) and solid oxide electrolytic cell (SOEC).[7–9]

Unlike ionic transport in sintering, creep and thermal migration, cations and anions in electrochemical devices always move in opposite directions: cations from anode to cathode, anions from cathode to anode. Such counter flow does not result in any "molecular" movement, so it should not lead to any inclusion migration. However, Kosevich, Geguzin, Krivoglaz and Lifshitz found that an inclusion can still migrate if the counter flows of oppositely charged ions go through two separate paths, e.g., one in the matrix and the other along the inclusion/matrix interface.[10] One example is illustrated in **Figure 1**, which depicts a pore in ZrO_2 having O^{2-} as the fast, leftward diffusing species flowing rapidly through the lattice, and Zr^{4+} as the slow, rightward diffusing species with localized flow limited to the surface. This allows ZrO_2 "molecules" to grow on the right and disappear from the left, thus the pore to move to the left.

Although the original theory of Kosevich et al. was formulated for an inclusion in an electric field E, we can generalize it to any counter-flow setting by expressing the predicted migration velocity, V_I, in terms of drift velocities v of counter ions along two separate paths.

$$V_I = 3\frac{\underline{v}^S_{Zr} v^L_O - \underline{v}^S_O v^L_{Zr}}{[(v^L_{Zr} + \underline{v}^S_{Zr}) + (v^L_O + \underline{v}^S_O)]} \quad (1)$$

In the above, the subscript (Zr or O) indicates the drift ion, the superscript (L for lattice/matrix or S for surface/interface) indicates the drift path, the underlined quantity carries a prefactor δ_s/r where δ_s is the thickness of the surface diffusion conduit and r the radius of the inclusion, and positive V_I implies migration in the direction of O^{2-} flow. The case depicted in Figure 1 thus corresponds to non-zero v^L_O and v^S_{Zr} but negligible v^S_O and v^L_{Zr}. Note that, without surface diffusion, $V_I = 0$. This reaffirms our earlier statement: inasmuch as lattice diffusion alone permits only opposite movement of O^{2-} and Zr^{4+}, it cannot result in any ZrO_2 movement.

Prof. I.-W. Chen, S.-W. Kim, Prof. J. Li
Department of Materials Science and Engineering
University of Pennsylvania
Philadelphia, PA 19104-6272, USA
E-mail: iweichen@seas.upenn.edu
S.-W. Kim, Prof. S.-J. L. Kang
Department of Materials Science and Engineering
Korea Advanced Institute of Science and Technology
Daejeon 305-701, Korea
Prof. F. Huang
State Key Laboratory of High Performance
Ceramics and Superfine Microstructures
Shanghai Institute of Ceramics
Chinese Academy of Sciences
Shanghai 200050, China

DOI: 10.1002/aenm.201200011

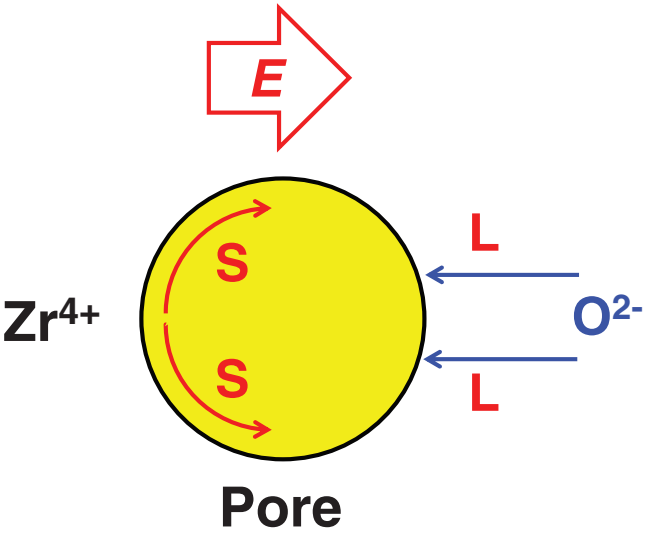

Figure 1. Schematic transport mechanism for pore movement. Flow of O^{2-} (ion wind) by lattice (L) diffusion meets flow of Zr^{4+} by surface (S) diffusion to deposit matter on the right side of a spherical or cylindrical pore. Electric field (*E*) pointing right.

The above picture is applicable to any counter-flow environment enabled by any driving force f ($v = (D/kT)f$, where D is the ion self diffusivity and kT has its usual meaning), so long as f points to opposite directions for oppositely charged ions. Electric field applied to a SOEC provides such a driving force, but so does oxygen potential field in a short-circuited SOFC (*no* electric field here).[11] In general, inclusion migration can proceed under any electrochemical force in an open system. (Closed systems, e.g., an open-circuited SOFC with a perfectly ionic electrolyte, have no transport, hence no inclusion movement.) To emphasize that an electric field is not a prerequisite for inclusion movement, we shall term the phenomenon *ionomigration*. Moreover, although the inclusion in Figure 1 follows the O^{2-} flow, for the opposite case of fast lattice Zr^{4+} diffusion and slow O^{2-} lattice diffusion, Equation (1) will predict inclusion migration to follow the Zr^{4+} flow. In this regard, ionomigration is driven by the prevailing ion "wind".

For perfectly ionic crystals, ionomigration of inclusions has only been observed in low melting-point (T_m) compounds (i.e., NaCl with T_m = 800 °C and LiF with T_m = 600 °C) electrically loaded at temperatures very close (within 50–100 °C) to T_m.[10] For widely used 8 mol% Y_2O_3-stabilized solid solution (8YSZ) and similar zirconia, ionomigration has never been suspected under normal SOFC/SOEC operating conditions (0.5–1 V, 800–1000 °C). This is despite the fact that these ceramics do contain pores[12–14] and certainly have robust O^{2-} flow. The reason is that zirconia is known to have a very stable microstructure, due to their very high T_m (2600 °C) and very low D_{Zr}^{L} (10^{12} times lower than D_O^L at 800–1000 °C).[15,16] Indeed, in similarly refractory UO_2 (T_m = 2850 °C), thermal migration of gas bubbles was observed only above 1800 °C.[4] Nevertheless, we have found rampant pore/bubble ionomigration in 8YSZ, accompanied by massive electro-sintering, at temperatures and voltages (e.g., 840 °C and 2 V) pertinent to electrochemical applications.

2. Results

2.1. Relative Motion of Pores/Bubbles vs Grain Boundaries Above 1250 °C

We recently reported pore relocation in initially 95% dense 8YSZ that was electrically loaded at 1350 °C for 10 h: the density of the anode half fell below 95% whereas that of the cathode half rose toward 100% (see Figure 8 of ref. [17]). We have repeated the above experiment using nearly dense samples that contain Ar bubbles. (See Figure S3a in the Supporting Information (SI) for initial microstructure of these samples.) Unlike pores, Ar bubbles cannot sinter; instead, their total volume will grow if they coalesce (a phenomenon well known in nuclear fuel).[4] In this way, Ar bubbles serve as "self-amplifying" markers. The micrograph of **Figure 2** for a Ar-containing sample, after loaded under an electric field $E = 5.3 \times 10^3$ V/m for 5 h at 1250 °C, shows bubbles along with distorted grain boundaries. The distortion indicates a relative motion: either bubble motion toward left or boundary motion toward right, or both. Some bubble-grain boundary breakaway is also apparent, leaving distorted boundaries in the wake.

Since grain boundary motion along E is possible in view of the electrically positive character of YSZ grain boundary,[18] Figure 2 is no proof of bubble ionomigration. (Pore relocation to the anode side mentioned earlier did suggest pore ionomigration toward anode.) But grain boundary movement is frozen below 1150° with or without electric loading,[17] so we repeated the above experiment around this threshold temperature. To ensure an accurate temperature measurement, we employed AC impedance spectroscopy as "in-situ thermometry" based on the following idea. Impedance spectroscopy can simultaneously measure the impedance of both the electrolyte (8YSZ) and the electrode. The electrode impedance typically changes over time because electrode's porous microstructure tends to evolve

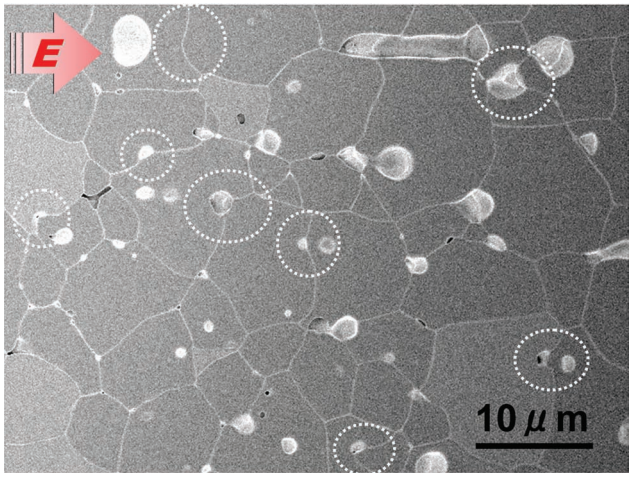

Figure 2. Migrating Ar bubbles in 8YSZ. Scanning electron micrograph (SEM) micrograph showing Ar bubbles, many elongated and some (circled) pulling the grain boundary toward left. Some bubbles have broken into two halves, one left inside the grain, the other pulling the grain boundary. $E = 5.3 \times 10^3$ V/m pointing right, 5 h at 1250 °C.

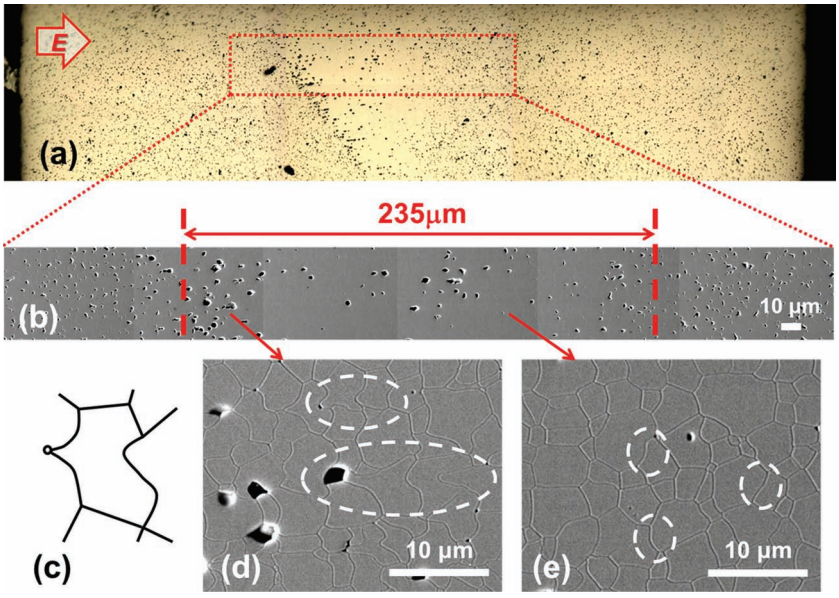

Figure 3. Localized zone of Ar bubble migration and grain boundary bowing. (a) Optical micrograph showing a cross section where bubbles have relocated and coalesced toward the left, with *E* pointing right. (b) A section of (a) viewed in SEM at a higher magnification. (c) Schematic for one migrating bubble passing through two opposing grain boundaries, causing distortion of both. (d) A region of (b) toward the left showing larger bubbles and severe grain boundary bowing (circled, per (c)). (e) Another region of (b) toward the right showing fewer, smaller bubbles with less grain boundary distortion (circled). Outside this zone the microstructure is the same as in the pristine material, SI, Figure S3a. (3.0 A/cm^2, 2.2 V at 1180 °C for 48 h, size: 1.68 mm^2 × 1.30 mm; sample 9 in SI, Table S1.)

under the combined influence of temperature and electric current,[9] but the YSZ impedance should remain constant unless its temperature changes due to Joule heating. (Joule heating was experienced in our prior work[17] and in the experiment for Figure 2.) In this way, the YSZ impedance measured by high-frequency impedance spectroscopy provides a direct reading of YSZ temperature. In SI, Figure S2 we determined the critical areal power density that causes Joule heating in our samples: the YSZ impedance began to fall when the power density exceeded ~8 W/cm^2. We then performed all the experiments described below with a power density less than the critical value and the YSZ impedance kept unchanged—before and during test—as verified by *in situ* spectroscopy. (See SI, Table S1 for a listing of sample configurations and test conditions.) To avoid electrolytic reduction of ZrO_2, which occurs at 2.15 V at 1000 °C in air, we also conducted all the experiments described below at less than this voltage (per four-point method).

2.2. Localized Bubble Migration at 1180 °C

At 1180 °C under 3.0 A/cm^2 (2.2 V across 1.3 mm, for 48 h), we were able to localize relative Ar-bubble/grain boundary movement to within a small zone of some 200 μm wide, **Figure 3**a-b. Within this well-defined zone, it is clear that bubbles had relocated, becoming accumulated on the left and depleted on the right (Figure 3a). Such redistribution cannot be explained by a rightward motion of grain boundaries, which should drag bubbles to the right; it can only result from a leftward motion of bubbles. As in Figure 2, severely contorted grain boundaries are numerous in the region of bubble accumulation (Figure 3d), some bubbles causing distortion of two opposing boundaries (schematic in Figure 3c); boundaries are less contorted in the region of bubble depletion, Figure 3e. This is also supported by the statistics of grain boundary distortion shown in SI, Figure S4a. As further shown in Figure S4b, we reproduced the above observation but with an expanded zone of relative bubble/boundary movement after increasing the current density but otherwise under nominally similar test conditions. (This latter sample experienced some Joule heating, so it is not listed in SI, Table S1.) Further increasing the current density or the temperature caused the zone to spread and engulf the entire sample, which had especially pronounced grain distortion and bubble accumulation near the anode.

Having established the connection between grain distortion and Ar bubble ionomigration, we reexamined air-sintered samples (initially 95% dense) under electric loading. Shortly before most pores were sintered away, we often found a localized zone on the anode side with a microstructure very similar to that of Figure 3d (data not shown). This indicates that air-filled pores also undergo ionomigration, although this can be observed only within a narrow space-time window because pores, contrary to Ar-bubbles, are "self-destructing" markers.

2.3. Electro-sintering at 840 °C

Pore/bubble migration under electric loading provides a new densification mechanism, at least for thin samples: porosity is removed by sweeping pores toward the anode, then exiting there. "Electro-sintering" is graphically illustrated in **Figure 4**a which is a cross section of a thin, air-fired 8YSZ disk of 70% initial density (see SI, Figure S3c for initial microstructure). The disk was Pt-electroded across the center section only, so that the ion flow was restricted to this section and did not extend to the rim section. This caused an hour-glass shape to develop after 24 h at 840 °C under ~0.5 A/cm^2 (1.9 V across 380 μm). The 29% thickness reduction of the center region relative to the rim region, which has no change in thickness, suggests the center region should have reached ~100%. Indeed, microscopy found the center fully dense (Figure 4b) and the rim unsintered (Figure 4c). Remarkably, the original grain size (0.22 μm) is maintained throughout the cross section. Since in fine grain ceramics densification and grain growth are normally controlled by the same diffusion process along the grain boundary, it is impossible to achieve full densification without grain coarsening in conventional sintering of pure ceramic or 8YSZ.[19] Yet this is readily accomplished by low-temperature electro-sintering giving an extremely fine grained 8YSZ ceramic, which is consistent with our picture that ionomigration is controlled by surface diffusion.

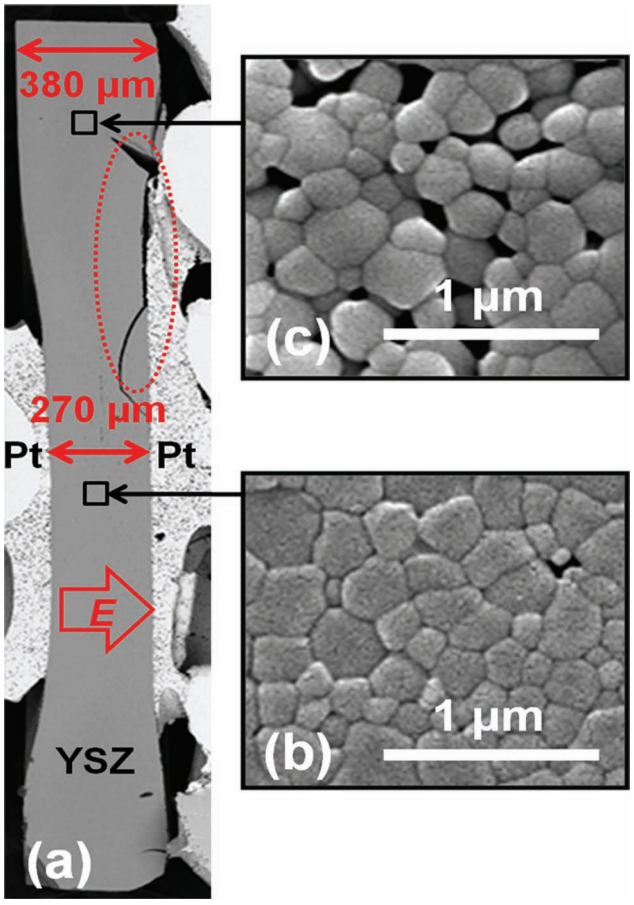

Figure 4. Electro-sintering of 8YSZ at 840 °C and 1.9 V. (a) SEM of hour-glass-shaped cross section undergoing electro-sintering in the center, with 29% thinning; the surrounding rim was not loaded, thus not sintered, having same thickness (380 μm) as before test. SEM for the center (b) and the rim (c) confirm electro-sintering without grain growth. In (a), YSZ is flatter on the right because of stronger constraint from the Pt cathode, which causes multiple cracking in (a) initiated at (upper right, circled) neck region at the YSZ/cathode interface. (0.5 A/cm^2 and 1.9 V for 24 h, 840 °C; sample 12 in SI, Table S1.)

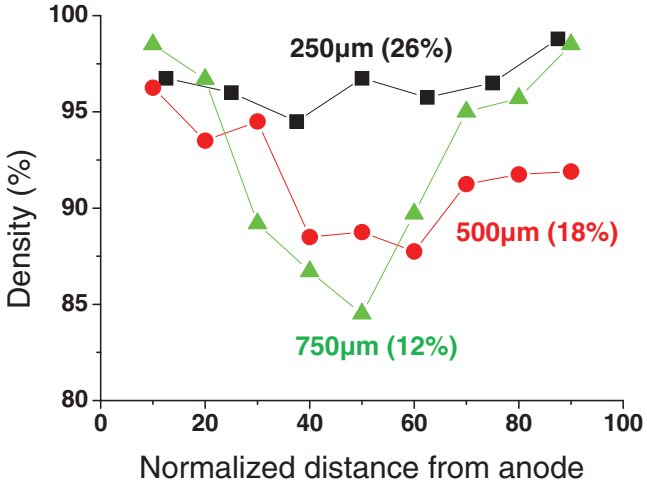

Figure 5. Thickness effect on electro-sintering and pore migration. Electro-sintering under the same electric field (40 V/cm), holding time (24 h) and temperature (850 °C), in samples of different thickness: 250 μm (squares), 500 μm (circles), and 750 μm (triangles). All three samples had a partial electrode configuration as in Figure 4a and showed hour-glass-shape cross sections after tests, from which thickness shrinkage due to electro-sintering was measured and indicated in% in parentheses next to the data lines; the latter plot density distributions (measured by counting porosity on the cross section using SEM) from anode to cathode. Sample 14–16 in SI, Table S1.

Electro-sintering and hour-glass-shaped cross sections were observed in other 840 °C tests with a similar electrode configuration, e.g., under ~0.3 A/cm^2 (1.2 V across 270 μm) for 24 h. With thinner samples (e.g., 270 μm and 380 μm), all pores disappeared throughout the thickness; with thicker samples (e.g., 500 and 750 μm), some pores remained in the mid-thickness section but not elsewhere (**Figure 5**). These results can be explained as follows. During their long journeys toward the anode some pores coalesced and became immobile (due to a size effect, to be described in the Discussion). This fate is most likely met by pores originating from the cathode side as they have the longest distance to travel; they tend to be trapped in the mid-thickness section.

2.4. Through-Thickness Bubble Migration at 875 °C

Because grain boundaries are immobile below 1150 °C, bubble/pore migration does not distort grain boundaries, making it difficult to discern bubble migration in nearly dense Ar-containing samples. However, using the same electrode configuration as in Figure 4a and making side-by-side comparisons of electroded and unelectroded regions in these samples, we detected strikingly different microstructures indicating grain boundary Ar-bubble-embrittlement occurring in unelectroded regions only. Embrittlement was evident throughout the 60 μm thick polished cross sections (**Figure 6**a) which showed numerous pits made of missing grains with sharp edges (Figure 6c). These edges are abrupt and flat, indicating grains had fallen apart because of poor cohesion and not plastic deformation or polish scratching. On the grain boundaries of the missing grains, many intergranular cavities reminiscent of creep-fracture cavities[20] are evident (lower left inset of Figure 6c, at a higher magnification). Apparently, these are Ar bubbles that grew by Oswald ripening during the 24 h hold at 875 °C, and it was their internal pressure that caused grain decohesion during polishing. In contrast, the electroded part, held at the same temperature and time but under 3.8 A/cm^2 (1.9 V across 60 μm), had a smooth polished section (Figure 6b) with all of the grains intact (Figure 6d, and the lower left inset at a higher magnification.) Having witnessed electro-sintering without grain growth at similar temperatures, we can attribute the smooth microstructure to ionomigration, which removed most bubbles from the sample thus preventing their accumulation at the grain boundaries, hence no embrittlement. A close-up examination shows most grains in Figure 6d do contain a few bubbles which were not there before testing (See initial microstructure in SI, Figure S3a). They are similar in size as grain boundary cavities in Figure 6c and probably came from bubble coalescence during ionomigration.

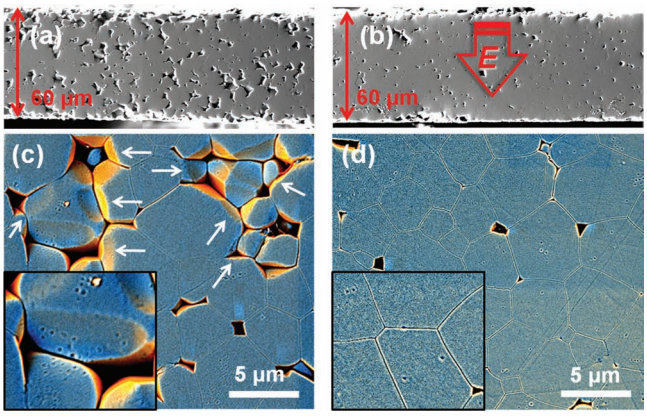

Figure 6. Bubble embrittlement vs escape at 875 °C. (a) Unelectroded region has pitted surface after polishing and suffers from (c) grains pullout (indicated by arrows) likely due to coalesced bubbles on grain boundaries (inset at lower left at higher magnification). (b) Electroded region has smooth surface after polishing with (d) no detached grains. Although most bubbles in (d) had apparently exited from anode, a few had coalesced and were left inside the grains (inset at lower left at higher magnification). Both (a) and (b) span the entire sample thickness. Color variations come from combining secondary electron detection with a positive bias (black to orange) and back scattered electron detection (black to blue), allowing enhanced contrast due to both topography and Zr/Y distribution. (3.8 A/cm^2, 1.9 V at 875 °C for 24 h; sample 1 in SI, Table S1.)

The above observations are relevant to SOFC and SOEC. SOEC sees an electric field that drives O^{2-} flow from cathode to anode; its voltage can approach the electrolytic limit, say 2 V. SOFC sees an electrochemical potential field that drives the same O^{2-} flow; the flow rate is at what would be generated by about 0.5 V, because the oxygen potential (the Nernst potential ~1.1 V) is opposed by an electric field that reduces the net potential to about ~50% of the Nernst potential when the cell is operating at the peak power. Since the 8YSZ membrane of these devices is typically less than 50 μm, even less than 1 μm in micro SOFC,[21] a very large O^{2-} wind is expected as are pore migration and electro-sintering. Direct evidence of these effects is difficult to detect because of the small thickness change and the absence of grain boundary distortion at low temperatures. However, pore accumulation in 8YSZ near the anode has been reported in SOEC[12] and SOFC,[13] which could be caused by ionomigration if pores and oxygen bubbles[14] cannot exit at the anode. Electro-sintering could be beneficial as it removes residual porosity, but the associated shrinkage stress could potentially cause cracking. Some interfacial debonding and cracking at the cathode/YSZ interface are indeed visible in Figure 4a (red circled). This scenario is supported by fracture mechanics analysis (Equations S1-S2 in the SI) which finds debonding to be energetically favorable at the electrode interface when 2% shrinkage is realized in a 10 μm thick 8YSZ. Such cracking can be avoided by using thinner membranes (like in micro SOFC) or more compliant electrodes.

3. Discussion

We have found bubble/pore migration and electro-sintering at temperatures well below what freezes grain boundary mobility, which is controlled by grain boundary Zr^{4+} diffusion. These results are consistent with Figure 1, which predicts it is surface Zr^{4+} diffusivity D_{Zr}^{S} (ignoring Y^{3+} for simplicity) that controls ionomigration and electro-sintering. Indeed, in the limit of fast O^{2-} diffusion and $r >> \delta_s$, Equation (1) reduces to

$$V_I = 3\left(\frac{\delta_S}{r}\right)\left(\frac{D_{Zr}^{S}}{kT}\right)4eE = 3\left(\frac{\delta_S}{r}\right)\left(\frac{D_{Zr}^{S}}{D_O^{L}}\right)\left(\frac{\Omega}{e}\right)i \qquad (2)$$

In the above, e is the charge of an electron, Ω is the volume of a ZrO_2 formula unit, D_O^L is lattice diffusivity of O^{2-}, and the second equality in terms of electric current density i is applicable to the general case of electrochemical diffusion dominated by O^{2-} flow.

Since Equation (2) predicts small bubbles/pores migrate faster, during any journey the distance traveled is mostly logged when the bubbles are small; when they collide and coalesce, they form bigger bubbles that then become dormant. From Figure 3a, we estimate $V_I = 1.36 \times 10^{-9}$ m/s from the width of the zone (235 μm) and the duration of the experiment (48 h, which is an overestimate of the travel time for small bubbles), at 1453 K and a nominal field $E = 1.69 \times 10^3$ V/m. (The nominal field is too an overestimate because a portion of the applied voltage is expended in the electrode, see the tables in the inset of Figure S2.) In Figure 6b, the estimated V_I from the thickness of the sample (60 μm) and the duration of the experiment (24 h, again an overestimate) is 6.94×10^{-10} m/s at 1148 K and $E = 30.8 \times 10^3$ V/m (also an overestimate). According to Equation (2) and assuming $\delta_s = \Omega^{1/3} = 0.31$ nm, for a bubble of $r = 0.025$ μm, these estimates give D_{Zr}^{S} of 1.8×10^{-12} m^2/s and 3.2×10^{-14} m^2/s, respectively, which are both underestimates. A similar estimate from another experiment at a higher temperature has also been made ($D_{Zr}^{S} = 3.7 \times 10^{-12}$ m^2/s at 1563 K), and all three results nicely follow an Arrhenius relation, $D_{Zr}^{S} = 2.8 \times 10^{-6} \exp(-174\ \text{kJ/mol}/RT)$ m^2/s, shown in **Figure 7**.

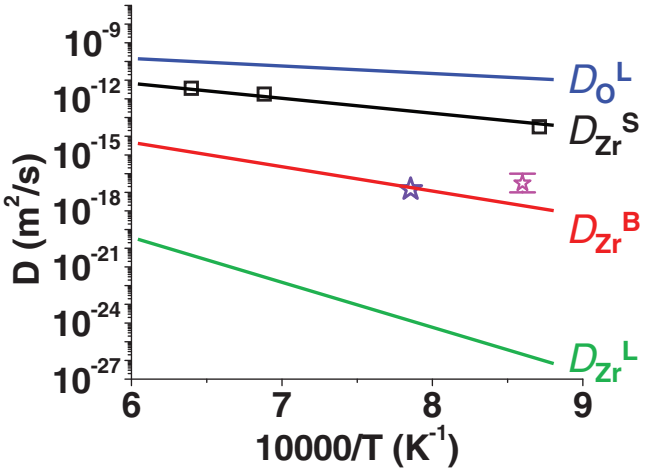

Figure 7. Arrhenius plot of surface diffusivities. Zr surface (S) diffusivity in this work, compared with its lattice (L)[16] and boundary (B)[22] diffusivities, and with O lattice diffusivity.[15] The only other D_{Zr}^{S} data (shown as stars) known for cubic zirconia were from in situ experiment (890 °C, with error band) on undoped ZrO_2 and grain boundary grooving experiment (1100 °C) on 8YSZ.[23]

Another estimate can be made by analyzing the sintering data using an anodic pore-exit model described by Equation S4, SI; it gives $D_{Zr}^{S} = 1.3 \times 10^{-5}$ exp(−154 kJ/mol/RT) m^2/s, which is 4.6 times faster. This difference can be attributed to the much smaller (more than 10 times) grain size in the electro-sintering experiment, which may affect the effective diffusivity. Note that D_{Zr}^{S} is smaller than $D_{O}^{L} = 3.0 \times 10^{-8}$ exp(−75 kJ/mol/RT) m^2/s,[15] consistent with our assumption in Figure 1. Meanwhile, D_{Zr}^{S} is much faster than Zr^{4+} diffusivity in the lattice, $D_{Zr}^{L} = 3.5 \times 10^{-5}$ exp(−478 kJ/mol/RT) m^2/s,[16] and in the grain boundary, $D_{Zr}^{B} = 9.6 \times 10^{-6}$ exp(−288 kJ/mol/RT) m^2/s.[22] Having a much smaller activation energy, D_{Zr}^{S} can remain active and enable ionomigration at much lower temperatures. (The reported data of D_{Zr}^{S} of cubic zirconia (one for undoped ZrO_2 at 890 °C, obtained by in situ observation of neck evolution inside a transmission electron microscope, the other for 8YSZ at 1000 °C, obtained by grain boundary grooving measuremetns on ceramic surfaces)[23] are somewhat lower, which could indicate electric enhancement of diffusion.[17])

Returning to the SOFC/SOEC and estimating V_I using D_{Zr}^{S}, we predict a $r = 0.025$ μm pore under 0.5 V can cross a 10 μm membrane of 8YSZ at 500 °C in 11 200 h, about one year. At 26% of T_m (3023 K) of YSZ, 500 °C is usually regarded too low for any microstructure instability. Yet ionomigration and electro-sintering may persist if lattice O^{2-}-wind is coupled to the very robust D_{Zr}^{S}, via inclusions. Thinner YSZ in micro SOFC can actually propel a large O^{2-} current i even at 300 °C.[21] Provided the ratio of $D_{Zr}^{S}/1388D_{O}^{L}$ remains favorable (the activation energy of D_{Zr}^{S} could decrease at lower temperatures, though), ionomigration may still be possible according to Equation (2).

Equation (2) predicts smaller pores/bubbles migrate faster. This explains pore/bubble coalescence in Figure 3a-b (small pores/bubbles catching up large ones) and residual porosity in Figure 5 (in the center sections of thicker electro-sintering samples, large coalescence-formed pores becoming immobile). As we believe ionomigration should occur in any electrochemical devices made of ionic conducting solids, it also predicts instability in such devices when the solids are nanocomposites (coalescence of initially well-dispersed second phase/pores).[24] The physical origin of the size effect is evident from Figure 1: as surface Zr^{4+} flows from the western hemisphere to the eastern hemisphere, it first passes through an annular ring of a perimeter $2\pi r$ and a "surface" thickness δ_s that separates the two hemispheres, it next spreads out to coat the eastern hemisphere which has an area $2\pi r^2$. The ratio of the ring area and the hemisphere area is thus reflected in the matter deposition rate, hence V_I, that scales as δ_s/r. This situation is most relevant in the low-temperature limit. In the high-temperature limit (e.g., above 1800 °C), evaporation and gas-phase transport of Zr^{4+} may dominate, which allow ion flow from the western hemisphere directly to the eastern hemisphere. This results in a size-independent V_I, which is not consistent with our experiments.

In electron/hole-conducting oxides such as $Co_{1-x}O$, which has frozen O^{2-}, pore migration under an oxygen potential gradient is controlled by cation lattice diffusion according to Martin and Schmalzried.[25] This conclusion was derived by assuming infinite v_O^S on the pore surface—a case that may be very appropriate for open porosity (instant surface oxidation).[26] Under this assumption, both their analysis and Equation (1) lead to $V_I = -3v_{Co}^{L}$, i.e., pore moves against the cation flow. Extending the same model to 8YSZ will require assuming infinite v_{Zr}^{S} on the pore/bubble surface, which leads to $V_I = 3v_O^L$. This predicted V_I has no size dependence and is much too fast to explain our data, so the model has to be rejected for our experiment.

Lastly, although it is the lattice O^{2-} wind that prevails in 8YSZ, Equation (1) does allow the opposing contribution from the lattice Zr^{4+} wind. The latter is given by the second term in the numerator of Equation (1), which corresponds to inclusion motion following the Zr^{4+} flow. Indeed, ionomigration always involves two opposite interdiffusion processes around an inclusion, and it is their imbalance (O^{2-} bulk diffusion coupled to Zr^{4+} interfacial diffusion *faster* than Zr^{4+} bulk diffusion coupled to O^{2-} interfacial diffusion) that results in a net movement. This is superficially reminiscent of the classical Kirkendall effect,[27–29] manifest as marker (an inert inclusion) movement caused by the imbalance of two opposing bulk diffusion fluxes on the same lattice, from which a vacancy wind results whose annihilation on preexisting defects causes the "sink-in" of the lattice and the translation of the entire crystal and the marker. In this respect, bubble migration in Figure 2–3 is analogous to marker movement, and the hour-glass distortion in Figure 4 is analogous to the translation of the external crystal boundary.

4. Conclusion

In summary, the interfacial diffusion-mediated ion-wind effect provides a new and intrinsically destabilizing mechanism for all ionic conducting solids: under a uniform electrochemical field, local short-circuit diffusion coupled to a global ion wind causes neutral second phase inclusions to migrate, resulting in a *kinetic* destabilization—phase aggregation, segregation, coarsening, densification—of even thermodynamically stable microstructures. Such ionomigration effects persisting to unexpectedly low temperatures and leaving unexpected benefit/damage challenge the presumption commonly held for ionic redox fuel/electrolysis cells and related solid-state devices: they have only one globally diffusing ionic species, thus they must be intrinsically stable. The inherent size dependence of ionomigration could also potentially compromise solid-state ionic nanostructures such as porous composite—based electrochemical devices[24] and thin film ionic switches.[30] For all these devices, reliability assessment using accelerated lifetime tests based on our linear V_I-i prediction may be advisable, preferably aided by a "tracer" such as Ar-bubbles described here.

5. Experimental Section

We prepared YSZ ceramics by spark plasma sintering (SPS), pressing 8YSZ powders (TZ-8Y, Tosoh Corporation, Tokyo, Japan) in a graphite die under 50 MPa in an Ar atmosphere (0.5 to 0.6 atm), at 1300 °C for 5 min. Decarburized (2 h in air at 1000 °C) ceramics were cut into squares (~1 mm sides) from 0.06 to 1.6 mm thick, to which platinum wires were attached using a platinum paste, then air fired (2 h at 1000 °C). The specimen was heated in air (840–1250 °C) and a constant DC voltage/current was used to maintain a current density for a prescribed time. Similar experiments using air-sintered YSZ of 95% (sintered at 1500 °C, for 2 h) and 70% (sintered at 1300 °C, with no holding)

were also conducted. The specimen temperature was monitored by an infrared pyrometer (M90-V, Mikron) and the voltage by the four-point-probe method. Time traces of current density, voltage and temperature of a representative experiment are shown in SI, Figure S1.

In-situ thermometry was provided by impedance spectroscopy (Gamry G750) in the four-point configuration from 10 μHz to 300 kHz. The results expressed in real and imaginary part of the impedance (Z) form one arc as in SI, Figure S2a, which includes several electric loading runs at a nominal temperature of 1100 °C. The left intersect of the arc with Re(Z) corresponds to the high frequency limit and is the Ohmic resistance of YSZ. The right intersect corresponds to the low frequency limit (~DC) and is the sum of all the resistances: Ohmic resistance of YSZ and electrodes, electrode activation, and impedance for gas diffusion and conversion.[12] As discussed in the SI, during electric-loading, although the right intersect typically changes with time and current as the porous electrodes evolve (all the arcs in SI, Figure S2a do) which affects all the non-YSZ (solid electrolyte) resistances, the left intersect remains constant until the YSZ temperature is affected by electric loading (in SI, Figure S2a, the three low current arcs have the same left intersect) which occurs above a critical power areal density (in SI, Figure S2a, the intersects of the three high current arcs decrease with current/voltage/power). Therefore, it is possible to in-situ monitor the YSZ temperature using the left intersect. We verified this finding at several nominal temperatures. In SI, Figure S2b, the YSZ temperature is maintained at the nominal temperature, 840 °C, because the power areal density is kept low, as indicated by the same left intersects of all the arcs. All of the experiments/samples listed in SI, Table S1 were conducted below this critical power density, thus free of Joule heating.

Tested specimens were polished and thermally etched to reveal their microstructure which was characterized by light microscopy and SEM. Microstructural features including fraction and size of bubbles, the linear intercept grain size and the fraction of distorted grains were measured following the standard stereological procedures.[31] Representative samples are listed in SI, Table S1 along with their configurations and test conditions (all of them below critical power density). For comparison, the starting microstructures of these materials (SPS, 95% dense and 70% dense) are shown in SI, Figure S3.

Supporting Information

Supporting Information is available from the Wiley Online Library or from the author.

Acknowledgements

This work was funded by the US Department of Energy (BES Grant No. DE-FG02-11ER46814) and used the facilities supported by the National Science Foundation (Grant Nos. DMR-11-20901). SWK acknowledges support of the Priority Research Center Program (Grant No. 2010-0029713) of Korea and the Brain Korea 21 program. JL acknowledges support by the Air Force Office of Scientific Research FA9550-08-1-0325.

Competing financial interest: The authors declare no competing financial interests.

Received: January 3, 2012
Published online: May 21, 2012

[1] a) K.-C. Chen, W.-W. Wu, C.-N. Liao, L.-J. Chen, K. N. Tu, *Science.* **2008**, *321*, 1066–1069; b) For applications, see H. Park, A. K. L. Lim, A. P. Alivisatos, P. L. McEuen, *Appl. Phys. Lett.* **1999**, *75*, 301–303; c) For a comprehensive review, see P. S. Ho, T. Kwok, *Rep. Prog. Phys.* **1989**, *52*, 301–348.

[2] H. Morton, *Friedman, Principles and Models of Biological Transport*, 2nd ed., Springer Verlag, Berlin, Germany **2008**.

[3] G. Gamba, *Physiological Review.* **2005**, *85*, 423–493.

[4] a) F. A. Nichols, *J. Nucl. Mater.* **1979**, *84*, 1–25; b) For a comprehensive review, see D. Olander, *Fundamental aspects of nuclear reactor fuel elements.*, Technical Information Center, ERDA, Springfield, Virginia, USA TID-26711-P1, **1976**.

[5] Y. Tsori, F. Yournilhac, L. Liebler, *Nature* **2004**, *430*, 544–547.

[6] a) D. G. Grier, *Nature* **2003**, *424*, 810–816; b) D. Psaltis, S. R. Quake, C. Yang, *Nature* **2006**, *442*, 381–386.

[7] T. Suzuki, Z. Hasan, Y. Funahashi, T. Yamaguchi, Y. Fujishiro, M. Awano, *Science* **2009**, *325*, 852–855.

[8] S. Park, J. M. Vohs, R. J. Gorte, *Nature* **2000**, *404*, 265–267.

[9] A. Hauch, S. D. Ebbesen, S. H. Jensen, M. Mogensen, *J. Mater. Chem.* **2008**, *18*, 2331–2340.

[10] a) A. M. Kosevich, *Soviet Phys.-Solid State.* **1965**, *7*, 360–365; b) I. M. Lifshitz, A. M. Kossevich, Ya. E. Geguzen, *J. Phys. Chem. Solids.* **1967**, *28*, 783–798; c) Ya. E. Geguzin, N. N. Ovcharenko, S. S. Simeonov, *J. Phys. Chem. Solids.* **1973**, *34*, 2059–2068; d) For a comprehensive treatise, see Ya. Geguzin, M. A. Krivoglaz, *Migration of Macroscopic Inclusions in Solids*, Consultants Bureau, New York-London **1973**.

[11] M. Martin, *Solid State Ionics.* 2000, *136–137*, 331–337.

[12] R. Knibbe, M. L. Traulsen, A. Hauch, S. D. Ebbesen, M. Mogensen, *J. Electrochem. Soc.* 2010, *157*, B1209-B1217.

[13] Y. Matus, L. C. De Jonghe, X.-F. Zhang, S. J. Visco, C. P. Jacobson, in Proceedings of the Eighth International Symposium on Solid Oxide Fuel Cells (SOFC VIII),Paris, France (Eds: C. Singhal, M. Dokiya), *Electrochemical Society Proceedings*, **2003**, *7*, 209.

[14] A. V. Virkar, *J. Am. Ceram. Soc.* **1990**, *73*, 3382–90.

[15] M. Kilo, C. Argirusis, G. Borchardt, R. A. Jackson, *Phys. Chem. Chem. Phys.* **2003**, *5*, 2219–2224.

[16] M. Kilo, G. Borchardt, B. Lesage, O. Kaitasov, S. Weber, S. Scherrer, *J. Europ. Ceram. Soc.* **2000**, *20*, 2069–2077.

[17] S.-W. Kim, S. G. Kim, J.-I. Jung, S.-J. L. Kang, I.-W. Chen, *J. Am. Ceram. Soc.* **2011**, *94*, 4231-4238.

[18] S.-L. Huang, I.-W. Chen, *J. Amer. Ceram. Soc.* **1990**, *73*, 3269–3277.

[19] a) I.-W. Chen, X.-H. Wang, *Nature* **2000**, *404*, 168–171; b) For 8YSZ, also see M. Mazaheri, Z. R. Hesabi, F. Golestani-Fard, S. Mollazadeh, S. Jafari, S. K. Sadrnezhaad, *J. Amer. Ceramic Soc.* **2009**, *92*, 990–995.

[20] I.-W. Chen, A. S. Argon, *Acta Merall.* **1981**, *29*, 1321–1333.

[21] a) A. Shao, S. M. Haile, J. Ahn, P. D. Ronney, Z. Zhan, S. A. Barnett, *Nature* **2005**, *435*, 795–798; b) H. Huang, M. Nakamura, P. C. Su, R. Fasching, Y. Saito, F. B. Prinz, *J. Electrochem. Soc.* 2007, *154*, B20-B24; c) A. Bieberle-Hutter, D. Beckel, A. Infortuna, U. P. Muecke, J. M. Rupp, L. J. Gauckler, S. Rey-Mermet, P. Muralt, N. R. Bieri, N. Hotz, M. J. Stutz, D. Poulikakos, P. Heeb, P. Muller, A. Bernard, R. Gmur, T. Hocker, *J. Power Sources.* **2008**, *177*, 123–130.

[22] I.-W. Chen, L. A. Xue, *J. Am. Ceram. Soc.* **1990**, *73*, 2585–2609.

[23] a) J. Rankin, B. W. Sheldon, *Mater. Sci. Eng.* **1995**, *204*, 48–53; b) K. A. Erk, C. Deschaseauz, R. W. Trice, *J. Amer. Ceram. Soc.* **2006**, *89*, 1673–1678.

[24] Y.-M. Chiang, *Science* **2010**, *330*, 1485–1486.

[25] M. Martin, H. Schmalzried, *Ber. Bunsenges. Phys. Chem.* **1985**, *89*, 124–130.

[26] H.-I. Yoo, K.-C. Lee, *J. Electrochem. Soc.* **1998**, *145*, 4243–4247.

[27] A. D. Smigelskas, E. O. Kirkendall, *Trans. AIME* **1947**, *171*, 130–142.

[28] Y. Yin, R. M. Rioux, C. K. Erdonmez, S. Hughes, G. A. Somorjai, A. P. Alivisatos, *Science* **2004**, *304*, 711–714.

[29] H. J. Fan, M. Knez, R. Scholz, K. Mielsch, E. Pippel, D. Hesse, M. Zacharias, U. Goesele, *Nature Mater.* **2006**, *5*, 628–631.

[30] R. Waser, R. Dittmann, G. Staikov, K. Szot, *Adv. Mater.* **2009**, *21*, 2632–2663.

[31] E. Underwood, *Quantitative Stereology*, Addison-Wesley Pub. Reading, MA, USA **1970**.